Multisublevel magnetoquantum conductance in single and coupled double quantum wires

S. K. Lyo
Sandia National Laboratories, Albuquerque, New Mexico 87185

Danhong Huang
Air Force Research Laboratory (AFRL/VSSS), Kirtland Air Force Base, New Mexico 87117

(Received 8 January 2001; published 31 August 2001)

We study the ballistic and diffusive magnetoquantum transport using a typical quantum point contact geometry for single and tunnel-coupled double wires that are wide ($\lesssim 1$ μm) in one perpendicular direction with densely populated sublevels and extremely confined in the other perpendicular (i.e., growth) direction. A general analytic solution to the Boltzmann equation is presented for multisublevel elastic scattering at low temperatures. The solution is employed to study interesting magnetic-field dependent behavior of the conductance such as a large enhancement and quantum oscillations of the conductance for various structures and field orientations. These phenomena originate from the following field-induced properties: magnetic confinement, displacement of the initial- and final-state wave functions for scattering, variation of the Fermi velocities, mass enhancement, depopulation of the sublevels and anticrossing (in double quantum wires). The magnetoconductance is strikingly different in long diffusive (or rough, dirty) wires from the quantized conductance in short ballistic (or clean) wires. Numerical results obtained for the rectangular confinement potentials in the growth direction are satisfactorily interpreted in terms of the analytic solutions based on harmonic confinement potentials. Some of the predicted features of the field-dependent diffusive and quantized conductances are consistent with recent data from GaAs/Al_xGa_{1-x}As double quantum wires.

DOI: 10.1103/PhysRevB.64.115320 PACS number(s): 73.40.Gk, 72.20.My, 72.20.Fr, 73.40.Kp

I. INTRODUCTION

Much attention has recently been focused on the low temperature ballistic quantum transport through a single narrow constricted channel (or wire), the so-called quantum point contact,[1–3] and also tunnel-coupled double wires.[4–7] The quantum ballistic conductance of these wires exhibits many interesting properties.[1] These wires are very thin in one direction and wide (e.g., $\lesssim 1$ μm) in the other direction perpendicular to the wire, producing dense sublevels. In this paper, we show that the diffusive conductance of these structures exhibits many interesting field-dependent properties, strikingly different from those of the ballistic conductance.

A single-channel quantum point contact is schematically shown in Fig. 1(a). This channel consists of an electron gas, for example, in a thin highly conducting GaAs layer ($\sim$100 Å) confined between Al_xGa_{1-x}As layers in the growth (z) direction. The current flows in the y direction through a narrow quasi-one-dimensional (1D) wire region which is formed by further constricting the current in the perpendicular (x) direction by applying a negative bias in the split metallic gate on top of the Al_xGa_{1-x}As layer as shown in Fig. 1(a). In this structure, only the ground sublevel is occupied in the z direction. However, the confinement in the x direction is much less severe, producing many closely separated sublevels (to be defined as channel sublevels). For a channel width of the order of a μm, the energy separation for the low-lying sublevels is a small fraction of an meV. The energy dispersion curves of these sublevels are illustrated in Fig. 1(b). As is well known, the conductance decreases in quantum steps of $2e^2/h$ in the ballistic regime as the bias becomes more negative, due to the depopulation of the channel sublevels. Similar monotonic quantized conductance steps were observed as a function of a perpendicular magnetic field.[2,3]

Recently, the effect of interlayer tunneling has been studied in a tunnel-coupled double channel structure illustrated in Fig. 1(c).[4–7] In this structure, the two GaAs conducting channels are separated by a thin Al_xGa_{1-x}As barrier which allows the electrons to tunnel between the two GaAs channels. The channel constriction in the x direction is achieved in both channels independently through top and bottom split gates, which allow probing both the 2D-2D, 2D-1D, and 1D-1D regimes by adjusting the gate biases.[4] Electron tunneling deforms the electronic structure in the channel direction dramatically in the presence of a magnetic field B in the x direction due to the anticrossing effect as illustrated in Fig. 1(d).[8–10] Here the thick solid curves represent the lower and upper branches of the tunnel-split ground-state doublet separated by the anticrossing gap in the z direction for the ground channel sublevel $n=0$. Basically, these branches are made of two ground-state parabolas from each well which are displaced by $\delta k \propto B$ in k space relative to each other, with the degeneracy lifted at the intersecting point and the curves near this point deformed by the anticrossing gap as shown.[9] The humps in Fig. 1(d), develop at a sufficiently high B.[9] The gap passes through the chemical potential as B increases. The thin curves are replicas of these curves: each pair represents a higher channel sublevel $n=1,2,\ldots$. A recent calculation predicted,[5] for this coupled double-wire structure, that the ballistic conductance shows a V-shaped quantum staircase and decreases in steps of $2e^2/h$ as a function of the field, reaches a minimum and then increases and saturates at high fields in agreement with the observed data.[4]

When the ballistic conductance does not show clear quantized behavior due to thermal or level broadening, it is not

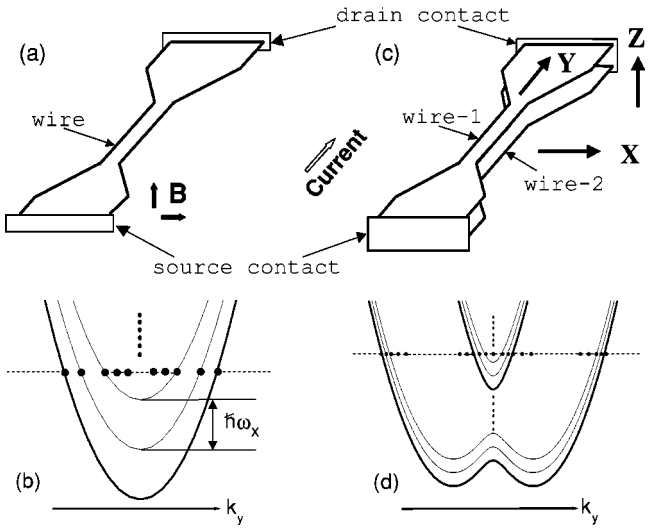

FIG. 1. (a) A schematic diagram of a single quantum wire. The narrow channel is formed by applying a negative bias on the top split metallic gate, not shown. (b) Parallel energy-dispersion curves of the channel sublevels of a single quantum wire. The levels belong to the ground sublevel from the z confinement. (c) Double quantum wires. Electrons tunnel between the wires through the $Al_xGa_{1-x}As$ barrier in the z direction. (d) The energy-dispersion curves of tunnel-coupled symmetric double QW's. The tunnel-split ground doublet for the ground $(n=0)$ channel sublevel is shown in thick curves for upper and lower branches. The thin curves (including the higher-energy levels represented by the vertical dots) are replicas of these curves shifted uniformly by $\hbar\omega_x$ in the harmonic channel confinement model and belong to the ground doublet. The horizontal black dots represent the Fermi points. The current flows in the y direction. A magnetic field **B** is in the x direction for the double wires and is either in the x or z direction for the single wire.

possible to determine if the electronic motion is ballistic or diffusive at zero magnetic field. Therefore it is interesting to calculate the field dependence of the conductance in the two limits. We find that, apart from the quantum steps, these two regimes show strikingly different B-dependent behavior of the conductance due to the magnetic confinement and displacement of the initial- and final-state wave functions for scattering, variation of the Fermi velocity, field-induced mass enhancement, depopulation of the sublevels and the field-induced anticrossing (in double quantum wires). The case of double-quantum wires is especially interesting, because the diffusive conductance is enhanced gigantically when the chemical potential lies in the anticrossing gap at a moderate B in the extreme quantum limit. In this limit, only the ground channel sublevel and the ground tunnel-split doublet are occupied due to extreme confinements in both x and z directions.[11–13] In wide double quantum wells (QW's) with densely populated channel sublevels, however, we find only a moderate enhancement of the conductance.

The Boltzmann equation involves elastic scattering among the Fermi points. The number of the Fermi points decreases monotonically as a function of B in single QW's, but in double QW's increases after a minimum and saturates at high fields. Each of the states at the Fermi points generates a rate equation. We show that these coupled equations form an overcomplete set of equations and are not linearly independent when the number of the Fermi points is finite. A formalism is developed for a general solution which is obtained by eliminating a redundant equation. The effect of weak localization and many-body effects are ignored in this paper.

The organization of this paper is as follows. In Sec. II, we present a formalism to calculate the conductance of multisublevel magnetotransport of electrons in quantum wire systems using the Boltzmann equation in the presence of impurity or interface-roughness scattering. Formal expressions are given for the impurity and interface-roughness scattering matrix in Sec. III for single and tunnel-coupled double quantum wires in a magnetic field, assuming a parabolic channel confinement which is employed throughout the paper. The scattering matrix elements are calculated for a single QW when the magnetic field is applied in the two perpendicular directions to the wire, further assuming a parabolic confinement in the growth direction in Sec. IV. An explicit expression is given for the scattering matrix elements for double quantum wires in a magnetic field for a general z confinement in Sec. V. The field dependence of the diffusive conductance is evaluated numerically in Sec. VI using rectangular z confinements and is compared with that of the ballistic conductance for various single-well and double-well structures. The numerical results are interpreted in terms of the analytic results based on the harmonic z confinement. Comparison is made with available data. The paper is summarized in Sec. VII with discussions.

II. MULTISUBLEVEL MAGNETOTRANSPORT

In this paper, we consider two systems consisting of either single or tunnel-coupled double quantum wires schematically illustrated in Fig. 1. The Boltzmann equation for the magnetotransport of electrons along the y direction is given by[14]

$$v_j+\frac{2\pi}{\hbar}\sum_{j'}|V_{j',j}|^2(g_{j'}-g_j)\,\delta(\mathcal{E}_j-\mathcal{E}_{j'})=0. \qquad (1)$$

Here $j=\{n,m,k\}$ represents a set of quantum numbers, where $n,m(=0,1,\ldots)$ are the channel-sublevel quantum number and the sublevel index associated with the quantization in the x and z directions, respectively, $\mathcal{E}_j$ is the energy of the electron and $v_j=\hbar^{-1}d\mathcal{E}_j/dk$ is the group velocity along the wire. We do not assume $\mathcal{E}(-k)=\mathcal{E}(k)$.[15] Here k is the wave number along the y direction. In general, $\epsilon(-k)\neq\epsilon(k)$ for asymmetric double quantum wipes in Fig. 1(d). The quantity g_j describes the component of the nonequilibrium distribution function $f_j=f_0(\mathcal{E}_j)+g_j[-f_0'(\mathcal{E}_j)]eE$, where the second term represents the linear deviation from the equilibrium distribution function $f_0(\mathcal{E}_j)$. Here E is the dc field and $f_0'(\mathcal{E})$ is the first derivative of the Fermi function. In our numerical application, only the ground sublevel $m=0$ is occupied for single quantum wires. For double quantum wires, the tunnel-split ground doublet $m=0,1$ are occupied. In Eq. (1), $V_{j',j}$ is the scattering matrix in the Born approximation. The Born approximation is valid in the present situ-

ation where the channel sublevels are densely separated. However, in the extremely narrow double-quantum-well channel where the channel sublevel spacing is much larger than the anticrossing gap, higher order corrections to the Born approximation can be significant when the Fermi level lies inside the gap.[12,13] The effect of the magnetic field is contained in the eigenvalues $\mathcal{E}_j$, wave functions, and the chemical potential as will become clear later.

The conductance equals

$$G_{yy}(B)=\frac{2e^2}{L_y^2}\sum_j v_j g_j \int_0^{+\infty} d\mathcal{E}\,\delta(\mathcal{E}_j-\mathcal{E})[-f_0'(\mathcal{E})]$$
$$=\frac{2e^2}{hL_y}\int_0^{+\infty} d\mathcal{E}[-f_0'(\mathcal{E})]\sum_{\nu=1}^{N_F} s_\nu g_\nu, \tag{2}$$

where L_y is the length of quantum wires and $s_\nu=v_\nu/|v_\nu|=\pm 1$. The k summation accompanying the j summation in Eq. (2) is replaced by $(L_y/h)\int(1/|v_j|)d\mathcal{E}_j$, yielding the second equality. The well-known cancellation of the current operator v_j and the one-dimensional density of states factor $1/|v_j|$ is responsible for the sign $s_j=v_j/|v_j|$ in the final expression in Eq. (2). Here, ν represents each intersecting point of the energy parameter $\mathcal{E}$ with the dispersion curve described by the quantum numbers n,m. These points become the Fermi points with $\{n_F,m_F,k_F\}$ at zero temperature. The set of the quantum numbers $\{n,m,k\}$ at the energy $\mathcal{E}$ will still be called the ''Fermi points'' for convenience hereafter. The quantities s_ν and g_ν are uniquely determined for each $\mathcal{E}$. The total number of the ''Fermi points'' N_F is a large even number and a function of B. At zero temperature, Eq. (2) yields

$$G_{yy}(B)=\frac{2e^2}{hL_y}\sum_{\nu=1}^{N_F} s_\nu g_\nu, \tag{3}$$

where the signs $s_\nu=\pm 1$ are paired at the Fermi points on the same dispersion curve. The ballistic quantized conductance[1] $\tilde{G}_{yy}(B)=2e^2N_F/h$ is obtained by setting the mean-free path at each Fermi point equal to the maximum value $s_\nu g_\nu=L_y$ in Eq. (3).

Equation (1) can be rewritten after carrying out the k integration as

$$s_\nu+\sum_{\nu'=1}^{N_F} u_{\nu,\nu'}(g_{\nu'}-g_\nu)=0, \tag{4}$$

where $\mathbf{u}$ is an $N_F\times N_F$ symmetric scattering matrix with the off-diagonal elements given by

$$u_{\nu,\nu'}=u_{\nu',\nu}=\frac{L_y}{\hbar^2}\frac{|V_{\nu'\nu}|^2}{|v_{\nu'}v_\nu|} \quad \text{for} \quad \nu\neq\nu'. \tag{5}$$

By defining the diagonal elements for $\underline{\mathbf{u}}$ as

$$u_{\nu,\nu}=-\sum_{\nu'\neq\nu} u_{\nu,\nu'}, \tag{6}$$

and introducing the column vectors

$$\mathbf{g}=\begin{bmatrix} g_1 \\ g_2 \\ \vdots \\ g_{N_F}\end{bmatrix} \quad \text{and} \quad \mathbf{s}=\begin{bmatrix} s_1 \\ s_2 \\ \vdots \\ s_{N_F}\end{bmatrix}, \tag{7}$$

we can cast Eq. (4) into a linear matrix equation

$$\underline{\mathbf{u}}\mathbf{g}=-\mathbf{s}. \tag{8}$$

Unfortunately, the coupled equations (of order N_F) in Eq. (8) cannot be solved by simply inverting $\mathbf{g}=-\mathbf{u}^{-1}\mathbf{s}$, because $\mathbf{u}$ does not have an inverse (i.e., $\det\mathbf{u}=0$). This is easily demonstrated by showing that the sum of all the rows of $\mathbf{u}$ vanishes for each column. Namely the rows are not linearly independent. To avoid this problem, we discard the last row in Eq. (8) and obtain the N_F-1 coupled equations:

$$\underline{\mathbf{U}}\mathbf{G}+g_{N_F}\mathbf{U}_{N_F}=-\mathbf{S}. \tag{9}$$

Here $\mathbf{U}$ is a $(N_F-1)\times(N_F-1)$ submatrix obtained by discarding the last row and the last column of $\mathbf{u}$, $\mathbf{U}_{N_F}$ is the last column vector of $\mathbf{u}$ without the last element, and $\mathbf{S}$, $\mathbf{G}$ are obtained from $\mathbf{s}$, $\mathbf{g}$ by truncating the last elements s_{N_F} and g_{N_F}, respectively:

$$\mathbf{U}_{N_F}=\begin{bmatrix} u_{1,N_F} \\ u_{2,\,N_F} \\ \vdots \\ u_{N_F-1,N_F}\end{bmatrix}, \quad \mathbf{S}=\begin{bmatrix} s_1 \\ s_2 \\ \vdots \\ s_{N_F-1}\end{bmatrix},$$

and (10)

$$\mathbf{G}=\begin{bmatrix} g_1 \\ s_2 \\ \vdots \\ g_{N_F-1}\end{bmatrix}.$$

Further introducing a new column vector

$$\mathbf{G}'=\begin{bmatrix} g_1' \\ g_2' \\ \vdots \\ g_{N_F-1}'\end{bmatrix}=\mathbf{G}-g_{N_F}\begin{bmatrix} 1 \\ 1 \\ \vdots \\ 1\end{bmatrix}, \tag{11}$$

we obtain from Eq. (9)

$$\underline{\mathbf{U}}\mathbf{G}'=-\mathbf{S}, \tag{12}$$

yielding $\mathbf{G}'=-\mathbf{U}^{-1}\mathbf{S}$.

The solution $\mathbf{G}'$ in Eq. (12) does not include the as-yet undetermined parameter g_{N_F}. However, this does not pose any problem because the conductance in Eq. (2) turns out to be independent of this undetermined parameter as will be

shown in the following. Replacing **G** by **G**′ through the relationship in Eq. (11) and using $s_1+s_2+\cdots+s_{N_F}=0$ for a general electronic structure which is a continuous function of k, we find $\Sigma_{\nu=1}^{N_F} s_\nu g_\nu = \mathbf{S}^\dagger \mathbf{G}'$ for the last term in Eq. (2) and therefore

$$G_{yy}(B) = -\frac{2e^2}{hL_y}\int_0^{+\infty} d\mathcal{E}[-f_0'(\mathcal{E})]\mathbf{S}^\dagger \underline{\mathbf{U}}^{-1}\mathbf{S}. \tag{13}$$

In Eq. (13), $\mathbf{S}^\dagger$ is the transpose of **S**. The final expression on the right-hand side of Eq. (13) does not include any unknown parameter.

III. SCATTERING MATRIX

The square of the scattering matrix is defined as a configuration average over the distribution of the scattering centers, i.e.,

$$|V_{j',j}|^2 = \langle\langle |\langle j'|V(\mathbf{r})|j\rangle|^2\rangle\rangle_{\rm av}, \tag{14}$$

where $V(\mathbf{r})$ is the scattering potential from impurities or the interface roughness.

A. Impurity scattering

For impurities with very short interaction range, the scattering potential takes the form

$$V(\mathbf{r}) = U_0\Omega_0 \sum_i \delta(\mathbf{r}-\mathbf{r}_i), \tag{15}$$

where $\mathbf{r}_i$ is the position vector of impurities. In Eq. (15), $V(\mathbf{r})$ has the strength U_0 inside a small local volume Ω_0 and vanishes outside. The impurities are further assumed to be distributed over two sheets at $z=z_1$ and $z=z_2$ and uniformly within the xy plane. Inserting Eq. (15) into Eq. (14) and using Eq. (5), we find

$$u_{j',j} = \frac{n_I\Omega_0^2U_0^2}{\hbar^2|v_jv_{j'}|}\int_{-\infty}^{+\infty} dx|\phi_{n'}(x)\phi_n(x)|^2 \times \sum_{i=1,2} c_i|\xi_{m'k'}(z_i)\xi_{mk}(z_i)|^2, \tag{16}$$

where n_I is the impurity density, c_i is the fractional distribution with $c_1+c_2=1$, $\phi_n(x)$ and $\xi_{mk}(z)$ are the x and z component of the electron wave functions in quantum wires.

B. Interface-roughness scattering

For interface roughness, the scattering potential is[12,16]

$$V(\mathbf{r}) = \sum_i V_i\delta b_i(\mathbf{r}_\parallel)\delta(z-z_i), \tag{17}$$

where V_i is the conduction band offset at the ith interface at $z=z_i$, $\delta b_i(\mathbf{r}_\parallel)$ is the layer fluctuation, and $\mathbf{r}_\parallel$ is the position vector within the xy plane. Introducing the correlation lengths according to

$$\langle\langle \delta b_i(\mathbf{r}_\parallel)\delta b_{i'}(\mathbf{r}_\parallel')\rangle\rangle_{\rm av} = \delta_{i,i'}\delta b_i^2 \exp\left[-\frac{(x-x')^2}{\Lambda_x^2}\right] \times \exp\left[-\frac{(y-y')^2}{\Lambda_y^2}\right], \tag{18}$$

and using Eqs. (5) and (14), we find

$$u_{j',j} = \frac{\sqrt{\pi}\Lambda_y}{\hbar^2|v_jv_{j'}|}\exp\left[-\frac{1}{4}(k-k')^2\Lambda_y^2\right] \times \int_{-\infty}^{+\infty} dx\,\phi_{n'}^*(x)\phi_n(x)\int_{-\infty}^{+\infty} dx'\,\phi_{n'}(x')\phi_n^*(x') \times \exp\left(-\frac{(x'-x)^2}{\Lambda_x^2}\right)\sum_i |V_i\delta b_i\xi_{m'k'}(z_i)\xi_{mk}(z_i)|^2, \tag{19}$$

where δb_i is the average layer fluctuation, and Λ_x and Λ_y are the correlation lengths in the x and y directions. The approximation in Eq. (18) is valid for wide wells. For narrow wells, the layer fluctuation $\delta b_i(\mathbf{r}_\parallel)$ should be treated as steplike potentials. The result in Eq. (19) reduces to Eq. (16) in the limit $\Lambda_x,\Lambda_y\to 0$ and $\pi\Lambda_x\Lambda_yV_i^2\delta b_i^2 = n_I\Omega_0^2V_0^2c_i$. For this reason, we consider only the interface-roughness scattering for numerical applications hereafter.

The matrix element $u_{j',j}$ in Eqs. (16) and (19) diverges when the chemical potential lies at the bottom of the band (i.e., $v_j=0$). This divergence (associated with the divergence of the density of states) is avoided by introducing a level-broadening parameter γ_ν at the bottom of the band for νth Fermi point, which yields

$$\frac{1}{v_\nu} = \begin{cases} (m_\nu^*/\gamma_\nu)^{1/2} & \text{if } 1/v_\nu > (m_\nu^*/\gamma_\nu)^{1/2}, \\ 1/v_\nu & \text{if } 1/v_\nu \leqslant (m_\nu^*/\gamma_\nu)^{1/2}, \end{cases} \tag{20}$$

where $m_\nu^* = \hbar^2(d^2\mathcal{E}_\nu/dk^2)^{-1}$ is the effective mass.

C. Parabolic channel confinement

In this paper, we assume a parabolic potential for the channel confinement with the Hamiltonian given by

$$\mathcal{H}_x = -\frac{\hbar^2}{2m_W}\frac{\partial^2}{\partial x^2} + \frac{1}{2}m_W\omega_x^2x^2. \tag{21}$$

The wave function is given by

$$\phi_n(x) = (\sqrt{\pi}2^n n!\ell_x)^{-1/2}\exp(-x^2/2\ell_x^2)H_n(x/\ell_x), \tag{22}$$

where $H_n(x)$ is the nth-order Hermite polynomial and $l_x=\sqrt{\hbar/m_W\omega_x}$. The eigenvalues are given by $\mathcal{E}_n^x=(n+1/2)\hbar\omega_x$ with $n=0,1,2,\ldots$.

The x' integration in Eq. (19) can be carried out by employing Eq. (22). We find[17]

$$u_{j',j}=\frac{\sqrt{\pi}\alpha_x\Lambda_y}{\hbar^2|v_j v_{j'}|}\mathcal{A}_{nn'}^2\exp\left[-\frac{1}{4}(k-k')^2\Lambda_y^2\right]\sum_{p=0}^{n_<}2^p p!C_{n,p}C_{n',p}(1-\alpha_x^2)^{(n+n')/2-p}\sum_i|V_i\delta b_i\xi_{m'k'}(z_i)\xi_{mk}(z_i)|^2$$
$$\times\int_{-\infty}^{+\infty}dx H_{n'}(x)H_n(x)H_{n+n'-2p}\left(\frac{\alpha_x^2\lambda_x^2 x}{\sqrt{1-\alpha_x^2}}\right)\exp[-\{1+(1-\alpha_x^2\lambda_x^2)\lambda_x^2\}x^2], \tag{23}$$

where $\lambda_x=\ell_x/\Lambda_x$, $\alpha_x=1/\sqrt{1+\lambda_x^2}$, $\mathcal{A}_{nn'}=(2^{n+n'}n!n'!\pi)^{-1/2}$, $n_<=\min(n,n')$, and $C_{n,p}=p!/n!(n-p)!$ is the binomial expansion coefficient. We can perform the integration in Eq. (23) using the fact that $\hbar\omega_x$ is usually very small. For example, for $\hbar\omega_x=0.1$ meV and $m_W=0.067$ (in units of the free electron mass m_0), we estimate $\ell_x=1.066\times10^3$ Å$\gg\Lambda_x$. In this limit we have $\lambda_x\gg1,\alpha_x\ll1$ and find[17]

$$u_{j',j}=\frac{\Lambda_x\Lambda_y}{\hbar^2\ell_x|v_j v_{j'}|}\mathcal{A}_{nn'}^2\exp\left[-\frac{1}{4}(k-k')^2\Lambda_y^2\right]\sum_i|V_i\delta b_i\xi_{m'k'}(z_i)\xi_{mk}(z_i)|^2\sum_{p=0}^{n_<}p!C_{n,p}C_{n',p}$$
$$\times\exp(-\alpha_x^2[(n+n')/2-p])2^{n+n'-1/2}\Gamma(p+\tfrac{1}{2})\Gamma(n-p+\tfrac{1}{2})\Gamma(n'-p+\tfrac{1}{2}), \tag{24}$$

where $\Gamma(x)$ is the gamma function.

IV. SINGLE QUANTUM WIRE

We assume that the magnetic field $\mathbf{B}=(B_x,0,B_z)$ is perpendicular to the wire with the vector potential given by $\mathbf{A}=(0,A_y,0)$ and $A_y=-B_x z+B_z x$. The Hamiltonian is given by

$$\mathcal{H}=-\frac{\hbar^2}{2}\frac{\partial}{\partial z}\left[\frac{1}{m^*(z)}\frac{\partial}{\partial z}\right]+U_{\mathrm{SQW}}(z)+\mathcal{H}_x+\frac{\hbar^2}{2m^*(z)}\left(k+\frac{eA_y}{\hbar}\right)^2, \tag{25}$$

where $\mathcal{H}_x$ is defined in Eq. (21), the last term is the kinetic energy along the wire, and $U_{\mathrm{SQW}}(z)$ is the single-quantum-well potential which is zero inside the well and V_0 outside. The well width is L_z and $m^*(z)$ is the electron effective mass which equals m_W and m_B inside the well and the barriers, respectively. The Zeeman energy is neglected.

A. B‖x

When **B** is in the x direction (i.e., $B=B_x$), we find $\mathcal{H}=\mathcal{H}_x+\mathcal{H}_z$ with

$$\mathcal{H}_z=-\frac{\hbar^2}{2}\frac{\partial}{\partial z}\left[\frac{1}{m^*(z)}\frac{\partial}{\partial z}\right]+U_{\mathrm{SQW}}(z)+\frac{\hbar^2}{2m^*(z)}\left(k-\frac{z}{\ell_c^2}\right)^2. \tag{26}$$

Defining $\mathcal{H}_z\xi_{mk}(z)=\mathcal{E}_{mk}^z\xi_{mk}(z)$ and employing $m^*(z)=m_W, U_{SQW}(z)=m_W\omega_z^2z^2/2$ for the quantum-well confinement, the quantized electron energy is given by

$$\mathcal{E}_j=\left(n+\frac{1}{2}\right)\hbar\omega_x+\left(m+\frac{1}{2}\right)\hbar\Omega_z+\frac{\hbar^2k^2}{2m^{**}}, \tag{27}$$

where $n,m=0,1,2,\cdots$, $m^{**}=m_W/[1-(\omega_c/\Omega_z)^2]$, $\omega_c=eB/m_W$, and $\Omega_z=\sqrt{\omega_c^2+\omega_z^2}$. The wave function $\xi_{mk}(z)$ is given by

$$\xi_{mk}(z)=(\sqrt{\pi}2^m m!\ell_{cz})^{-1/2}\exp[-(z-\Delta z_k)^2/2\ell_{cz}^2]\times H_m[(z-\Delta z_k)/\ell_{cz}], \tag{28}$$

where $\ell_{cz}=\sqrt{\hbar/m_W\Omega_z}$ and $\Delta z_k=k\ell_c^2(\omega_c/\Omega_z)^2$ with $\ell_c=\sqrt{\hbar/eB}$. We note from Eq. (27) that the electron effective mass m^{**} becomes heavier for transport in the y direction and the sublevel separation $\hbar\Omega_z$ increases with B. Heavier mass increases the density-of-states and therefore decreases N_F.

The scattering matrix $u_{j',j}$ is given by the expression in Eq. (24) which contains the factor $\xi_{m'k'}(z_i)\xi_{mk}(z_i)$. However, according to Eq. (28), the centers of these initial- and final-state wave functions are shifted by $\Delta z_{k'}=k'\ell_c^2(\omega_c/\Omega_z)^2$ and $\Delta z_k=k\ell_c^2(\omega_c/\Omega_z)^2$, respectively. Since the signs of k' and k are opposite for the back-scattering processes responsible for the momentum dissipation, these magnetic displacements reduce the overlap between the initial and final states exponentially and enhance the conductance. For the back scattering $k'=-k$, for example, the product becomes $\xi_{m'k'}(z_i)\xi_{mk}(z_i)\propto\exp(-F(B))$ where $F(B)=(z_i/\ell_{cz})^2+(\Delta z_k/\ell_{cz})^2$. The function $F(B)$ varies significantly as a function of B as can be seen from the following numerical estimate. For $B=10$ T (with $\ell_c=81.1$ Å), $m^*=0.067$, and $k=0.02$ Å^{-1}, for example, and $\hbar\omega_z\simeq\Delta\mathcal{E}=15.4$ meV (sample 1 in Table I), we find $\hbar\Omega_z=23.2$ meV, $\Delta z_k=73.1$ Å, $\ell_{cz}=70$ Å, and $F(B)=(z_i/70)^2+1.09$. For $B=0$, on the other hand, $\ell_{cz}=86$ Å and $F(0)=(z_i/86)^2$, yielding a large value $F(B)-F(0)=2.64$ for $z_i=150$ Å at the interface in sample 1. Note that the limiting behavior of the conductance is given approximately by $G_{yy}(B)\propto\exp[2F(B)]$ where $F(B)\propto B^2$ in the low-field limit ($\omega_c\ll\omega_z$) and $F(B)\propto B$ in the high-field limit ($\omega_c\gg\omega_z$). This point will be further illustrated in the numerical results in Sec. VI A.

TABLE I. Single-quantum-well wires with well depth of 280 meV, width L_z, ground-second level separation $\Delta\mathcal{E}$, and the uniform channel sublevel separation $\hbar\omega_x$.

Sample no.	L_z (Å)	$\Delta\mathcal{E}$ (meV)	$\hbar\omega_x$ (meV)
1	300	15.4	0.02
2	210	29.0	0.02
3	210	29.0	0.2
4	210	29.0	2

B. B‖z

When **B** lies in the z direction (i.e., $B=B_z$), it is convenient to write the Hamiltonian as $\mathcal{H}=\tilde{\mathcal{H}}_x+\tilde{\mathcal{H}}_z$, where

$$\tilde{\mathcal{H}}_x=-\frac{\hbar^2}{2m_W}\frac{\partial^2}{\partial x^2}+\frac{1}{2}m_W\Omega_x^2(x+\Delta x_k)^2+\frac{\hbar^2k^2}{2m^{**}}, \quad (29)$$

$$\tilde{\mathcal{H}}_z=-\frac{\hbar^2}{2}\frac{\partial}{\partial z}\left[\frac{1}{m^*(z)}\frac{\partial}{\partial z}\right]+U_{\mathrm{SQW}}(z), \quad (30)$$

where $\Omega_x=\sqrt{\omega_c^2+\omega_x^2}$, $\Delta x_k=k\ell_c^2(\omega_c/\Omega_x)^2$, and $m^{**}=m_W/[1-(\omega_c/\Omega_x)^2]$. The electron wave functions are obtained from $\tilde{\mathcal{H}}_x\phi_{nk}(x)=\mathcal{E}_{nk}^x\phi_{nk}(x)$ and $\tilde{\mathcal{H}}_z\xi_m(z)=\mathcal{E}_m^z\xi_m(z)$ with $\mathcal{E}_{nk}^x=(n+1/2)\hbar\Omega_x+\hbar^2k^2/2m^{**}$. Again, the electron effective mass in the y direction and the sublevel separation increase with B. For $m^*(z)=m_W, U_{SQW}(z)=m_W\omega_z^2z^2/2$, the quantized electron energy is

$$\mathcal{E}_j=\left(n+\frac{1}{2}\right)\hbar\Omega_x+\left(m+\frac{1}{2}\right)\hbar\omega_z+\frac{\hbar^2k^2}{2m^{**}}, \quad (31)$$

with $n,m=0,1,2,\ldots$. The eigenfunctions are given by

$$\begin{bmatrix}\phi_{nk}(x)\\ \xi_m(z)\end{bmatrix}=\begin{bmatrix}(\sqrt{\pi}2^n n!\ell_{cx})^{-1/2}\exp[-(x+\Delta x_k)^2/2\ell_{cx}^2]H_n[(x+\Delta x_k)/\ell_{cx}]\\ (\sqrt{\pi}2^m m!\ell_z)^{-1/2}\exp[-z^2/2\ell_z^2]H_m(z/\ell_z)\end{bmatrix}, \quad (32)$$

where $\ell_{cx}=\sqrt{\hbar/m_W\Omega_x}$ and $\ell_z=\sqrt{\hbar/m_W\omega_z}$. The center of the wave function $\phi_{nk}(x)$ is shifted by $-\Delta x_k$, yielding a field-induced reduction in the overlap of the initial and final scattering states similar to the **B**‖**x** case. When the correlation length Λ_x is very short, namely for $\Lambda_x\ll\ell_{cx}$, the scattering matrix in Eq. (19) can be calculated analytically using Eq. (32), yielding[17]

$$u_{j',j}=\frac{\Lambda_x\Lambda_y}{\hbar^2|v_jv_{j'}|\ell_{cx}}\exp\left[-\frac{1}{4}(k-k')^2\Lambda_y^2\right]\sum_i|V_i\delta b_i\xi_{m'}(z_i)\xi_m(z_i)|^2$$
$$\times\int_0^{+\infty}dq\cos(q\Delta x_{k'-k}/\ell_{cx})\exp\left(-\frac{1}{2}q^2\right)L_n\left(\frac{q^2}{2}\right)L_{n'}\left(\frac{q^2}{2}\right), \quad (33)$$

where $L_n(x)$ is the nth-order Laguerre polynomial. We assume that the interface roughness exists only on one of the two interfaces in GaAs/Al_xGa_{1-x}As single QW's (i.e., $\delta b_1\equiv\delta b, \delta b_2=0$). The B dependence of the conductance is very different from the **B**‖**x** case, as will be shown later in Sec. VI.

V. TUNNEL-COUPLED DOUBLE QUANTUM WIRES

For double quantum wires, a most interesting situation occurs when **B** is in the x direction (i.e., $B=B_x$). In this case, the Hamiltonian is the sum of $\mathcal{H}=\mathcal{H}_{\mathrm{DQW}}^z+\mathcal{H}_x$, where $\mathcal{H}_x$ was defined in Eq. (21) and

$$\mathcal{H}_{\mathrm{DQW}}^z=-\frac{\hbar^2}{2}\frac{\partial}{\partial z}\left[\frac{1}{m^*(z)}\frac{\partial}{\partial z}\right]+U_{\mathrm{DQW}}(z)$$
$$+\frac{\hbar^2}{2m^*(z)}\left(k-\frac{z}{\ell_c^2}\right)^2, \quad (34)$$

where $U_{\mathrm{DQW}}(z)$ is the double QW potential which is zero inside two wells with widths L_{z1} and L_{z2} and V_0 in the center barrier (with thickness L_B) as well as in the two outer barriers for GaAs/Al_xGa_{1-x}As double QW's. An intuitive understanding of the role of B in Eq. (34) is gained by using a tight-binding picture where the z-wave functions are localized in each well separated by an effective distance d_{eff}. Here d_{eff} is roughly the distance between the maxima of the wave functions of the two wells. In the absence of tunneling (in the z direction), the energy dispersion consists of two sets of an infinite number of parallel parabolas for each well, separated by the energy $\hbar\omega_x$. The net effect of the magnetic field in the last term of Eq. (34) is to shift the two sets of the energy-dispersion parabolas relative to each other by $\delta k=d_{\mathrm{eff}}/\ell_c^2$ along the wire direction in k space, producing points of intersection between these two sets of the parabolas. In particular, for each pair of the parabolas with the same quantum number n out of these two sets, an anticrossing gap opens when tunneling is switched on as shown in Fig. 1.

TABLE II. Double-quantum-well wires with well depth of 280 meV, widths L_{z1}, L_{z2}, center-barrier width L_B, ground-doublet tunnel splitting $\Delta_{\rm SAS}$ at $B=0$, and the uniform channel sublevel separation $\hbar\omega_x$.

Sample no.	L_{z1}/L_{z2} (Å)	L_B (Å)	$\Delta_{\rm SAS}$ (meV)	$\hbar\omega_x$ (meV)
5	80/80	50	1.6	0.02
6	80/80	50	1.6	0.2
7	80/80	40	3.3	0.02

These gaps pass through the chemical potential successively as B is increased,[5,9] producing interesting transport properties.

The wave functions are given by $\mathcal{H}_x\phi_n(x)=(n+\frac{1}{2})\hbar\omega_x\phi_n(x)$ and $\mathcal{H}^z_{\rm DQW}\xi_{mk}(z)=\mathcal{E}^z_{mk}\xi_{mk}(z)$, where $\phi_n(x)$ is defined in Eq. (22) and $\xi_{mk}(z)$ is calculated numerically using Eq. (34). A parabolic potential is no longer appropriate for the double-quantum-well electron confinement in the z direction. Only the two lowest tunnel-split doublet states with $m=0,1$ are occupied for the small well widths L_{z1} and L_{z2} considered here. The quantized electron energy is

$$\mathcal{E}_j=\left(n+\frac{1}{2}\right)\hbar\omega_x+\mathcal{E}_{mk}, \tag{35}$$

where $n,m=0,1,2,\ldots$. The eigenvalues in Eq. (35) are shown in Fig. 1. The two thick curves therein correspond to $\mathcal{E}_{mk}$ with $m=0$ (lower curve) and $m=1$ (upper curve). The scattering matrix $u_{j',j}$ is given by Eq. (23) in general and by Eq. (24) in the limit of $\ell_x \gg \Lambda_x$. The interface roughness is assumed to exist only at the two interfaces $i=1,2$ between the GaAs wells and the $Al_xGa_{1-x}As$ barriers in the growth sequence of GaAs/Al_xGa_{1-x}As double QW's with $\delta b_1=\delta b_2=\delta b$. As will be shown in Sec. VI, the anticrossing effect introduces strikingly different phenomena to the magnetotransport absent in single-wire structures.

VI. NUMERICAL RESULTS AND DISCUSSIONS

In our numerical calculations, we study the conductance ratio $G_{yy}(B)/G_{yy}(0)$ in the diffusive limit (relevant to long wires) as a function of magnetic field B in both single and tunnel-coupled double quantum wires in the presence of interface-roughness scattering. The quantized conductance $\tilde{G}_{yy}(B)$ is also displayed for short quantum wires not only for comparison but also for showing the number of the populated sublevels at each B. For single quantum wires, a uniform magnetic field is applied either in the x or z direction, perpendicular to the wires. For double quantum wires, the magnetic field lies always in the x direction. The effects of the well width, channel sublevel separation, electron density, center barrier thickness, and the temperature on $G_{yy}(B)/G_{yy}(0)$ and $\tilde{G}_{yy}(B)$ are investigated. The parameters employed for all the samples in our calculation are listed in Tables I and II. For these samples, we use $V_0=280$ meV, $m_W=0.067$, and $m_B=0.073$. The level-broadening parameters are chosen to be $\gamma_\nu=0.16$ meV for all single-quantum-wire samples and $\gamma_\nu=0.1\Delta_{\rm SAS}$ for symmetric double-quantum-wire samples where $\Delta_{\rm SAS}$ is the splitting between the symmetric and antisymmetric states at $B=0$. The other roughness-related parameters are $\Lambda_x=\Lambda_y=30$ Å and $\delta b=5$ Å. The single and double QW's are assumed to be rectangular wells in the z direction. For single quantum wires, the energy separation between the first and second sublevels at $B=0$ are denoted as $\Delta\mathcal{E}$ in Table I. In the following applications, only the ground sublevel and the ground tunnel-split doublet are populated for single and double wires, respectively.

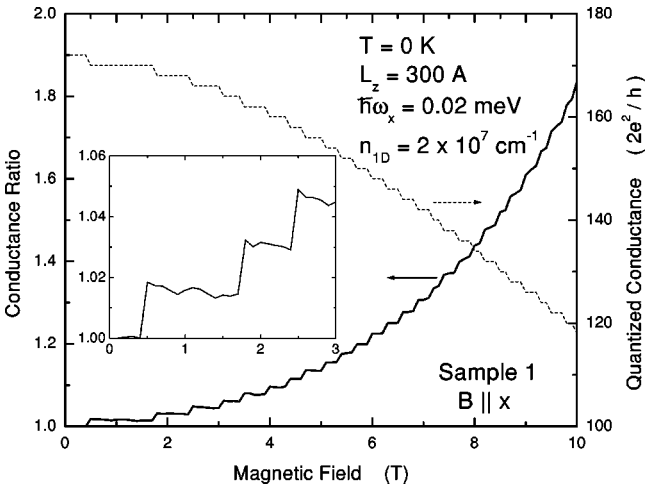

FIG. 2. $G_{yy}(B)/G_{yy}(0)$ (thick solid curve) and $\tilde{G}_{yy}(B)$ (thin dashed curve) for sample 1 with $n_{1D}=2\times10^7$ cm^{-1} at $T=0$ K as a function of B in the x direction. Here, $G_{yy}(0)=49.0e^2/h$ for $L_y=0.1$ mm. The inset displays the low-B behavior of $G_{yy}(B)/G_{yy}(0)$ for $0\leqslant B\leqslant 3$ T.

A. Single quantum wells

We display in Fig. 2 the diffusive conductance ratio $G_{yy}(B)/G_{yy}(0)$ (thick solid curve, left axis) and the quantized conductance $\tilde{G}_{yy}(B)$ (thin dashed curve, right axis) at $T=0$ K as a function of $\mathbf{B}\|\mathbf{x}$ for sample 1 with a linear density $n_{1D}=2\times10^7$ cm^{-1}. For this sample, the well width is large with a small level separation $\hbar\omega_z\sim\Delta\mathcal{E}=15.4$ meV (see Table I). All the occupied channel sublevels belong to the $m=0$ ground sublevel. A total of 85 channel sublevels are occupied at $B=0$ with 170 Fermi points.

Since $\tilde{G}_{yy}(B)$ is proportional to the total number of the Fermi points N_F and therefore the number of the occupied sublevels, the quantized conductance $\tilde{G}_{yy}(B)$ decreases in steps of $2e^2/h$ with increasing B owing to the fact that the effective mass m^{**} and thus the density of states (DOS) increases with B as seen from Eq. (27).[2] In contrast, the diffusive conductance $G_{yy}(B)/G_{yy}(0)$ increases exponentially in Fig. 2 as $\exp(c_1B^2)\approx1+c_1B^2$ in the low-B region and as $\exp(c_2B)\approx1+c_2B$ in the high-B region, where c_1 and c_2 are constants. The physical origin of this behavior was discussed in Sec. IV A. The high-B limit $\omega_c\geqslant\omega_z$ is reached at $B=8.9$ T. The enhancement of $G_{yy}(B)/G_{yy}(0)$ is much smaller in Fig. 3 because of larger $\hbar\omega_z$ (or smaller L_z). Os-

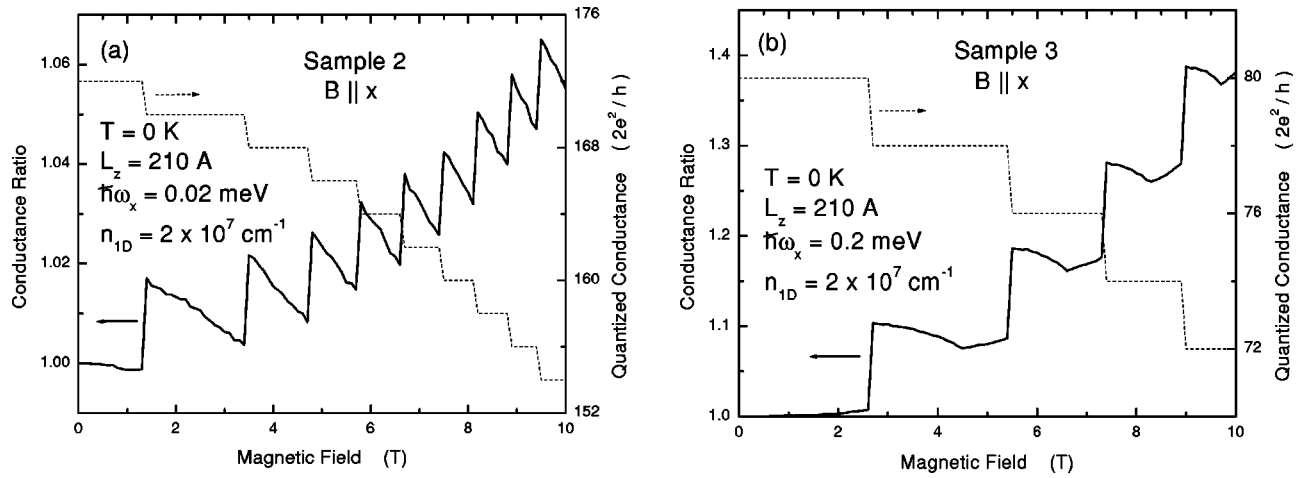

FIG. 3. $G_{yy}(B)/G_{yy}(0)$ (thick solid curve) and $\tilde{G}_{yy}(B)$ (thin dashed curve) for (a) sample 2 and (b) sample 3 with $n_{1D}=2\times10^7$ cm^{-1} at $T=0$ K as a function of B in the x direction. Here, $G_{yy}(0)=16.8e^2/h$ in (a) and $G_{yy}(0)=15.3e^2/h$ in (b) for $L_y=0.1$ mm.

cillations seen in the inset of the figure come from the successive depopulation of the sublevels as B increases. This oscillating feature is much more pronounced in samples with large ω_x as shown in Fig. 3(b) and will be examined in more detail below. Note also that the diffusive conductance cannot grow indefinitely. It reaches the maximum at the ballistic quantized conductance value and follows the B-dependent behavior of $\tilde{G}_{yy}(B)$ thereafter.

Figure 3 presents the conductance ratio $G_{yy}(B)/G_{yy}(0)$ (thick curves, left axis) and the quantized conductance $\tilde{G}_{yy}(B)$ (thin curves, right axis) at $T=0$ K as a function of $\mathbf{B}\|\mathbf{x}$ for samples 2 [in 3(a)] and 3 [in 3(b)] with $n_{1D}=2\times10^7$ cm^{-1}. A total of 86 channel sublevels are occupied at $B=0$ in sample 2 with $\hbar\omega_x=0.02$ meV. Sample 3 has much larger $\hbar\omega_x=0.2$ meV and contains only 40 occupied channel sublevels, producing a lower $\tilde{G}_{yy}(B)$ than sample 2. The plateaus in $\tilde{G}_{yy}(B)$ and the intervals between the abrupt jumps in $G_{yy}(B)/G_{yy}(0)$ coincide and indicate the intermediate stages between two successive depopulations and are much wider for sample 3 than for sample 2. The reduction of the plateau widths and the oscillation intervals for $G_{yy}(B)/G_{yy}(0)$ with increasing B reflects the increased density of states $\propto\sqrt{m^{**}}$ in each channel sublevel. The effective mass $m^{**}=m_W/[1-(\omega_c/\Omega_z)^2]$ was introduced in Eq. (27). The conductance $G_{yy}(B)/G_{yy}(0)$ in Fig. 3(a) decreases monotonically between the successive nearly discontinuous jumps. This behavior is explained in terms of a simple picture where the conductance is proportional to the sum of $v_k^2\rho_k\tau_k=|v_k|\tau_k$ on the Fermi surface with the DOS given by $\rho_k=1/v_k$. The transport relaxation time τ_k is the inverse of the weighted sum of the DOS over the Fermi points. The Fermi velocity $|v_k|$ decreases steadily as the Fermi point moves toward the bottom of the sublevel with increasing B, raising ρ_k and thereby decreasing τ_k and the conductance. The Fermi point near the bottom of the nearly empty top sublevel with $v_k\simeq0$ makes a negligible contribution to the current but contributes significantly to reducing τ_k through its large DOS. Namely, the electrons at other Fermi points are rapidly scattered into this Fermi point because of its large DOS $\rho_k=1/v_k$. The role of the damping parameter γ_ν is to avoid the divergence of ρ_k at $v_k=0$ and make τ_k and the conductance nonvanishing at the bottom of the band just before depopulation. When the top sublevel is depopulated, the DOS decreases abruptly, yielding a nearly discontinuous jump in τ_k and the conductance, leading to the sawtoothlike oscillating feature. The height of the jump scales as $1/N_F$ since the depopulation effect will be more significant when there are smaller number of sublevels, yielding larger jump heights for sample 3 compared to that of sample 2. Note that the vertical axes of these two curves have different scales. Apart from the oscillations, the average diffusive conductance increases quadratically in B as discussed for Fig. 2 through the B dependence of the scattering matrix $u_{j',j}$. The effect of the latter is reflected in the slow increase of $G_{yy}(B)/G_{yy}(0)$ in Fig. 3(b) between the slow decrease and the subsequent jump.

Figure 4 displays the conductance ratio $G_{yy}(B)/G_{yy}(0)$ (thick curves, left axis) and the quantized conductance $\tilde{G}_{yy}(B)$ (thin curves, right axis) as a function of $\mathbf{B}\|\mathbf{z}$ at $T=0$ K for sample 3 [Fig. 4(a)] and sample 4 [Fig. 4(b)] with low electron densities $n_{1D}=1\times10^6$ cm^{-1} (dashed curves) and 2×10^6cm^{-1} (solid curves). Sample 4 has much larger $\hbar\omega_x=2$ meV compared to $\hbar\omega_x=0.2$ meV of sample 3, allowing a relatively smaller number of the channel sublevels to be populated. The oscillating sawtoothlike features in $G_{yy}(B)/G_{yy}(0)$ are associated with the sublevel depopulation as in Fig. 3 and are much more pronounced for sample 4. In contrast to the $\mathbf{B}\|\mathbf{x}$ case in Fig. 3, however, the average $G_{yy}(B)/G_{yy}(0)$ in Fig. 4 (without the superimposed oscillations) decreases with B except for the initial steep rise near $B=0$. The origin of this drastically different behavior from the high-B behavior in Figs. 2 and 3 lies in the fact that the magnetic field in the z direction shrinks the channel orbit size ℓ_{cx} and increases the mass m^{**} in Eq. (29), thereby increasing $u_{j',j}\propto m^{**2}/\ell_{cx}$ according to Eq. (33) and decreasing $G_{yy}(B)/G_{yy}(0)$. The same behavior is not obtained for ℓ_{cz} for the $\mathbf{B}\|\mathbf{x}$ case because $\omega_z\gg\omega_x$. At low fields, namely in the limit $\omega_c\ll\omega_x$, dominant scattering occurs from $n=n'$. In

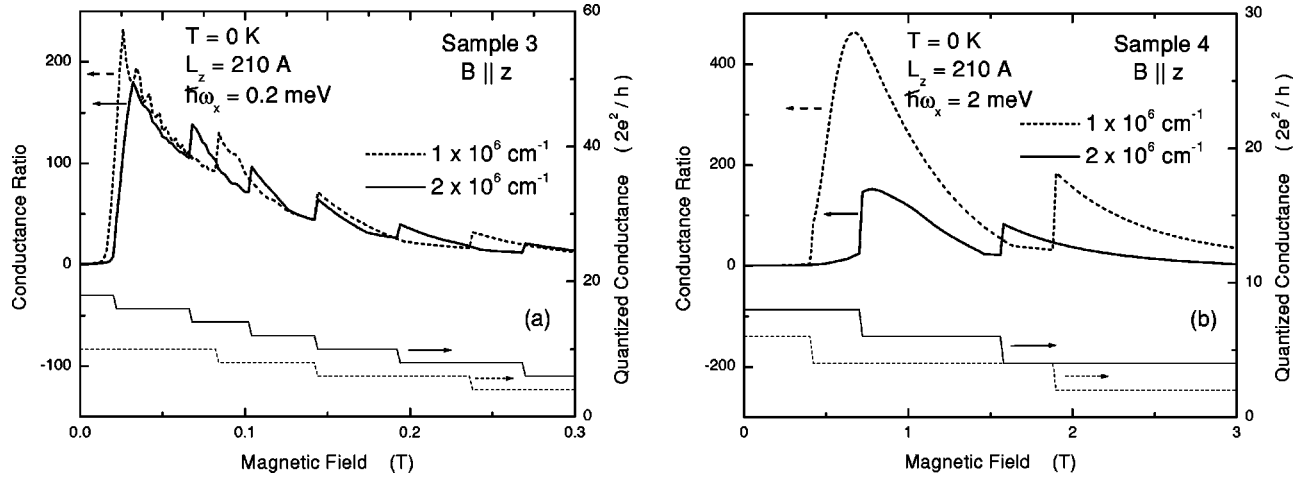

FIG. 4. $G_{yy}(B)/G_{yy}(0)$ (thick curves) and $\tilde{G}_{yy}(B)$ (thin curves) for (a) sample 3 and (b) sample 4 with $n_{1D}=1\times10^{6}$ cm^{-1} (dashed curves) and 2×10^{6} cm^{-1} (solid curves) at $T=0$ K as a function of B in the z direction. Here, $G_{yy}(0)=9.9e^2/h$ (dashed curve) and $15.5e^2/h$ (solid curve) in (a) and $G_{yy}(0)=4.2e^2/h$ (dashed curve) and $15.9e^2/h$ (solid curve) in (b) for $L_y=10$ μm.

this case, $u_{j',j}$ decreases rapidly with increasing B due to the B-induced relative displacement $\Delta x_{k'-k}$ of the initial and final wave functions, thereby increasing $G_{yy}(B)/G_{yy}(0)$ steeply as shown in Fig. 4. Eventually the shrinking orbit size increases the scattering matrix, resulting in the initial maximum in $G_{yy}(B)/G_{yy}(0)$. For the high-density sample 3 in Fig. 4(a) (thick solid curve), this initial steep rise of the conductance and the jump due to the first sublevel depopulation coincide. For sample 4 in Fig. 4(b), ω_x is too large, yielding only a small initial displacement $\Delta x_{k'-k}$, producing no significant initial rise of $G_{yy}(B)/G_{yy}(0)$. The small oscillations which follow the initial peak for sample 3 are due to the oscillating overlaps in the high-order Laguerre polynomials in Eq. (33) or the Hermite polynomials in Eq. (32) and Eq. (19). The oscillations are more visible for the low-density sample 3 (thick dashed curve). For the high-density sample (thick solid curve), n becomes too large and the oscillations smear out. These oscillations are absent for sample 4 in Fig. 4(b) due to the fact that large ω_x yields smaller number n of occupied sublevels and that low-order (n) Laguerre or Hermite polynomials oscillate less.

B. Double quantum wells

While the energy dispersion curves consist of a set of parallel parabolas in single QW's, they are given by a set of parallel anticrossing curves $\mathcal{E}_j$ introduced in Eq. (35) for double QW's, where $j=\{n,m,k\}$ with $m=0,1$. These curves are shown in Fig. 1(d) for the case where the magnetic field is in the x direction. The thick curves represent the ground-state doublet for $n=0$. The doublet consists of the upper ($m=1$) and the lower ($m=0$) branches (thick solid curves) separated by the partial gap. The thin curves (for $n=1,2,\ldots$) are the replicas of the thick curves. The gap associated with each n moves up and passes successively through the chemical potential with increasing B.[9] As will be shown in the following, the diffusive and quantized conductances show very different B-dependent behavior from that of the single QW's. It was found earlier for the extreme quantum limit (where only the ground channel sublevel $n=0$ is occupied) that higher-order corrections to the Born scattering can be significant for long-range scattering potentials when the chemical potential is inside the gap.[12] No such corrections are necessary for the present multiple-sublevel scattering.

We show in Fig. 5 the conductance ratio $G_{yy}(B)/G_{yy}(0)$

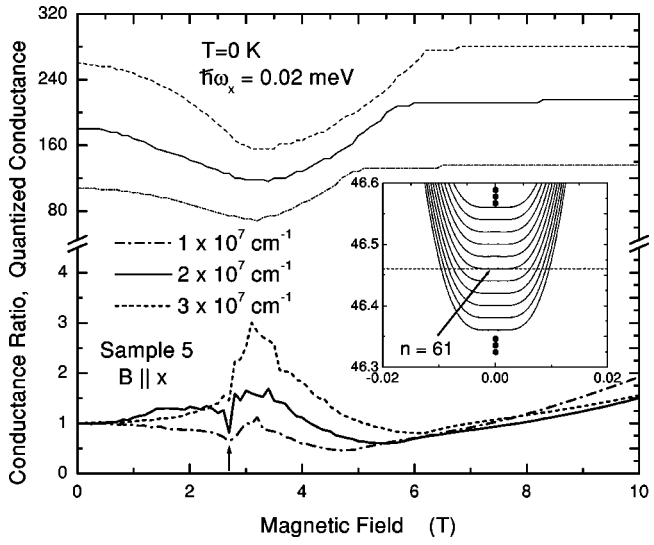

FIG. 5. $G_{yy}(B)/G_{yy}(0)$ (thick curves) and $\tilde{G}_{yy}(B)$ (thin curves) in unit of $2e^2/h$ for sample 5 with $n_{1D}=1\times10^{7}$ cm^{-1} (dash-dotted curves), 2×10^{7} cm^{-1} (solid curves) and 3×10^{7} cm^{-1} (dashed curves) at $T=0$ K as a function of B in the x direction. Here, $G_{yy}(0)=17.7e^2/h$ (thick dash-dotted curve), $28.4e^2/h$ (thick solid curve) and $32.5e^2/h$ (thick dashed curve) for $L_y=1$ μm. Both branches are occupied for solid and dashed curves, while only the lower branch is occupied for the dash-dotted curve at $B=0$. The arrow indicates the dips near $B=2.7$ T where the bottom of the lower branch becomes flat just before the hump develops as shown in the inset. The latter presents $\mathcal{E}_{n0k}$ in units of meV as a function of k (in 0.1πÅ^{-1}) at $B=2.7$ T. The horizontal dashed line indicates the Fermi level nested at the sublevel $n=61$.

(lower thick curves) and the quantized conductance $\tilde{G}_{yy}(B)$ (upper thin curves) at $T=0$ K as a function of B for sample 5 for several different electron densities $n_{1D}=1\times10^7$ cm^{-1} (dash-dotted curves), 2×10^7 cm^{-1} (solid curves), and 3×10^7 cm^{-1} (dashed curves). $\tilde{G}_{yy}(B)$ exhibits a V shape as a function of B. This B dependence was explained earlier in detail[5] and can be understood with the following simple argument. This argument is also useful for understanding the B dependence of the diffusive conductance to be presented below. At $B=0$, each $m=0,1$ pair of the doublet consists of two parallel parabolas and generates four Fermi points except for a few large-n top sublevels near the chemical potential, assuming a high density of electrons. As B increases, the upper and lower branches of each sublevel n deform from a pair of parallel parabolas into the anticrossing structure with a gap shown in Fig. 1 by thick curves, for example, for $n=0$. At high fields the gaps sweep through the chemical potential successively starting from large n. For each pair, the number of the Fermi points decreases from four to two when the chemical potential is in the gap and increases back to four when the gap moves above the chemical potential. Therefore, the minimum $\tilde{G}_{yy}(B)$ is obtained when the chemical potential lies in the middle of the anticrossing gaps of the majority of the channel sublevels. The minimum of $\tilde{G}_{yy}(B)$ shifts to a higher B for a higher-density sample.

It is interesting to note that the maximum of $G_{yy}(B)/G_{yy}(0)$ is aligned with the minimum of $\tilde{G}_{yy}(B)$ in Fig. 5 for each density. This behavior is readily understood if we first consider an extremely narrow channel where $\hbar\omega_x$ is very large and assume that only the ground $(n=0)$ doublet is occupied.[11] In this case, $\tilde{G}_{yy}(B)$ is minimum when the chemical potential lies inside the gap with two Fermi points as explained above. Also, the conductance becomes very large due to the fact that back scattering is suppressed between the two initial (k_i) and final $(k_f=-k_i$, say, in a symmetric structure) Fermi points in the lower branch $(m=0)$. For these two points, the wave functions $\xi_{mk_i}(z)$ and $\xi_{mk_f}(z)$ are localized in the opposite wells, yielding very small scattering matrix $u_{j',j}$ and a large conductance.[11] For a wide channel with many sublevels $(N_F\gg1)$ populated at high density, however, there are some sublevels for which the Fermi level is outside their gaps, although the majority of the sublevels have the Fermi level inside their gaps at the $\tilde{G}_{yy}(B)$ minimum. The wave functions of the Fermi points outside the gap have significant amplitudes in both wells, yielding large scattering matrices and reducing the enhancement.[11] Therefore, only a moderate enhancement is obtained for the diffusive conductance as shown in Fig. 5. This figure indicates that the effective back scattering is weakest, when the number of the Fermi points is minimum, yielding maximum $G_{yy}(B)/G_{yy}(0)$. The above B-induced separation of the initial and final scattering states and the concomitant weakening of the scattering rate is still significant for the Fermi points above the gaps of the sublevels at low B and is responsible for the initial rise of the diffusive conductance at high densities (thick solid and dashed curves). We note that the diffusive conductance shown by the thick dash-dotted curve for the lowest density decreases initially in contrast to the other two curves. This behavior occurs when only the lower branch is occupied at $B=0$ as will be studied in more detail later in this section. Note that the peak enhancement is larger for the thick dashed curve (with a larger electron density) than the thick solid curve because the chemical potential enters the gaps at higher B where the separation of the initial and final scattering states is more complete in the former case. The minimum of $G_{yy}(B)/G_{yy}(0)$ in the range $4.5<B<6.5T$ arises when the chemical potential passes through the last few humps in the lower branches with a large DOS, which increases the scattering rate. At high B where all the gaps are above the chemical potential, the two wells behave as independent single wells. Therefore $G_{yy}(B)/G_{yy}(0)$ increases gradually as a function of B as discussed in Figs. 2 and 3.

We also notice that $G_{yy}(B)/G_{yy}(0)$ has a dip at $B=2.7$ T in Fig. 5 indicated by an arrow. The position of the dip is insensitive to the electron density of the samples. This dip is associated with the flat bottoms of the lower branch of the dispersion curves of the sublevels (see the inset) which pin the Fermi level to the divergence in the DOS. The latter yields rapid scattering of the electrons and thus a small conductance. These flat bottoms are the consequence of the balanced competition between the B-induced rise of the crossing point arising from the increasing displacement δk $(=d_{\rm eff}/\ell_c^2)$ between the two parabolas and the downward repulsion from the upper level. These flat bottoms eventually develop into humps at higher fields.[9] Other rugged structures arise from the sublevel depopulation effect.

The effect of the thermal broadening is shown in Fig. 6. The parameters for Fig. 6(a) are the same as those from sample 5 studied in Fig. 5. The $T=0$ K quantum steps in $\tilde{G}_{yy}(B)$ (upper thin curves) and sharp structures in $G_{yy}(B)/G_{yy}(0)$ (lower thick curves) in Fig. 5 are significantly rounded at $T=0.3$ K as shown in Fig. 6(a). The effect of the thermal broadening is more clearly seen in Fig. 6(b) for sample 6 with much larger $\hbar\omega_x$ and a smaller density $n_{1D}=2\times10^6$ cm^{-1}. In this case, the bottom region of the upper branch is occupied in spite of the low density because $\hbar\omega_x$ is large requiring the occupation of fewer channel sublevels. For large $\hbar\omega_x=0.2$ meV, it was necessary to restrict our calculation to small densities in order to avoid large Fermi wave numbers, which require long computational times. The sublevel depopulation effect is clearly seen at 0 K from the dash-dotted curves for both the diffusive and quantized conductances. In particular, the sawtooth-like behavior of the diffusive conductance is similar to that in Figs. 3 and 4 of the single QW's.

We found in Figs. 5 and 6(a) that the diffusive conductance decreases with B initially when only the lower branch is populated, in contrast to the case where both branches are occupied. This effect is seen in Fig. 7 in samples 5 (solid curves) and 7 (dashed curves). These samples have the same density but sample 7 has smaller center-barrier width, yielding a much larger 3.3 meV gap compared with the 1.6 meV gap of sample 5. As a result, only the lower branch is occu-

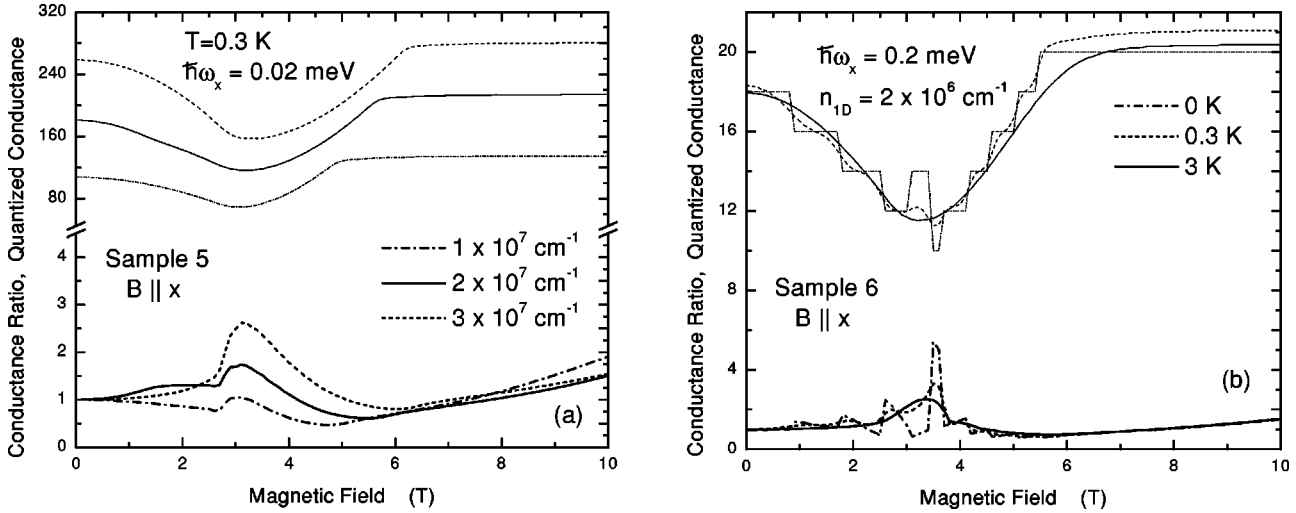

FIG. 6. $G_{yy}(B)/G_{yy}(0)$ (thick curves) and $\tilde{G}_{yy}(B)$ (thin curves) in unit of $2e^2/h$ for (a) sample 5 with $n_{1D}=1\times10^7$ cm^{-1} (dash-dot curves), 2×10^7 cm^{-1} (solid curves), and 3×10^7 cm^{-1} (dashed curves) at $T=0.3$ K and (b) for sample 6 with $n_{1D}=2\times10^6$ cm^{-1} at $T=0$ K (dash-dotted curves), 0.3 K (dashed curves), and 3.0 K (solid curves) as a function of B in the x direction. Here, $G_{yy}(0)=17.8e^2/h$ (thick dash-dotted curve), $28.2e^2/h$ (thick solid curve), and $32.8e^2/h$ (thick dashed curve) in (a) and $G_{yy}(0)=2.9e^2/h$ (thick dash-dotted curve), $3.0e^2/h$ (thick dashed curve), and $2.9e^2/h$ (thick solid curve) in (b) for $L_y=1$ μm.

pied in sample 7 while both branches are populated in sample 5. The basic features of the solid curves are similar to those in Fig. 5 and have already been explained. On the other hand, the quantized conductance (i.e., the number of the Fermi points) of sample 7 (thin dashed curve) drops very slowly initially with B. In this case, the argument presented for the V-shaped quantized conductance for the high-density case (where the number of the Fermi points changes from four to two and back to four with B) does not apply. The slow decrease arises from the fact that bottom region of the lower branch becomes flatter initially with increasing B, yielding a large DOS and requiring less channel sublevels to accommodate the electrons. This effect is also partially responsible for the reduction of the Fermi points in Fig. 5 for sample 5 and in Fig. 7 (thin solid curve). The increasing densities of states at the Fermi points in the lower branches also increase the scattering rates, lowering the diffusive conductance initially as shown by the thick dashed curve. In contrast, this mechanism has little effect on the low-B diffusive conductance for the high-density sample 5 in Fig. 7 because the curvatures of both upper and lower branches are negligibly affected at the Fermi points lying far above the gap. As discussed earlier, the B-induced localization of the eigen functions of the initial (k_i) and final ($k_f=-k_i$) states into the opposite wells weakens the back scattering eventually as discussed earlier, maximizing the conductance around $B=3.3$ T for the thick solid curve and $B=4.8$ T for the thick dashed curve. Note however that the maximum and minimum of the conductances are shifted to higher B for sample 7 (dashed curves) relative to those of sample 5 (solid curves). These shifts arise from the fact that the quantity B enters Eq. (34) approximately as a product $d_{\rm eff}B$. B is then scaled as $1/d_{\rm eff}$ which is larger for sample 7. An alternate explanation is that a larger B is required to form a fully developed anticrossing hump (see Fig. 1) because of the stronger repulsion (or tunneling) between the upper and lower branches in sample 7. This effect also explains the fact that the channel sublevels are initially depopulated faster in sample 5 than in sample 7 as seen from the more rapid initial decay of the quantized conductance of sample 5 due to more rapid diamagnetic rise of the sublevels.

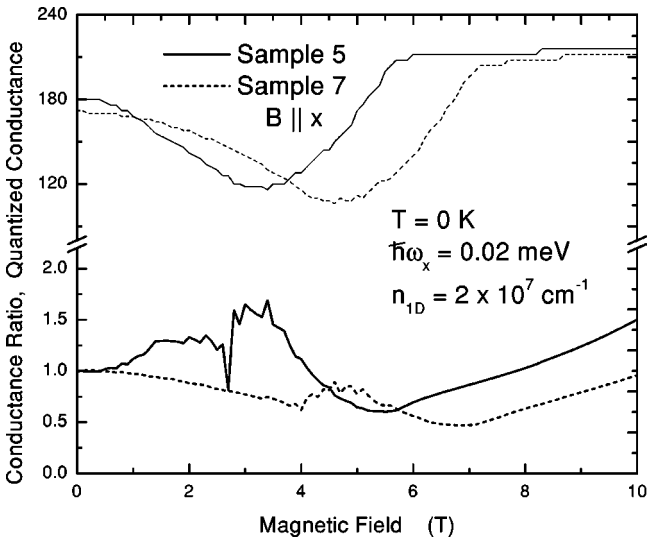

FIG. 7. $G_{yy}(B)/G_{yy}(0)$ (thick curves) and $\tilde{G}_{yy}(B)$ (thin curves) in unit of $2e^2/h$ for samples 5 (solid curves) and 7 (dashed curves) with $n_{1D}=2\times10^7$ cm^{-1} at $T=0$ K as a function of B in the x direction. Here, $G_{yy}(0)=33.9e^2/h$ (thick dashed curve) and $28.4e^2/h$ (thick solid curve) for $L_y=1$ μm. Sample 5 (sample 7) has a large 50 Å (small 40 Å) center-barrier width, a small 1.6 meV (large 3.3 meV) gap and has both branches (only the lower branch) populated at $B=0$.

In Fig. 8 we study the effect of the asymmetry of the double QW's at $T=0$ K using sample 5 with $n_{1D}=2\times10^7$ cm^{-1}, $\gamma_v=0.16$ meV, biasing the sample with dc

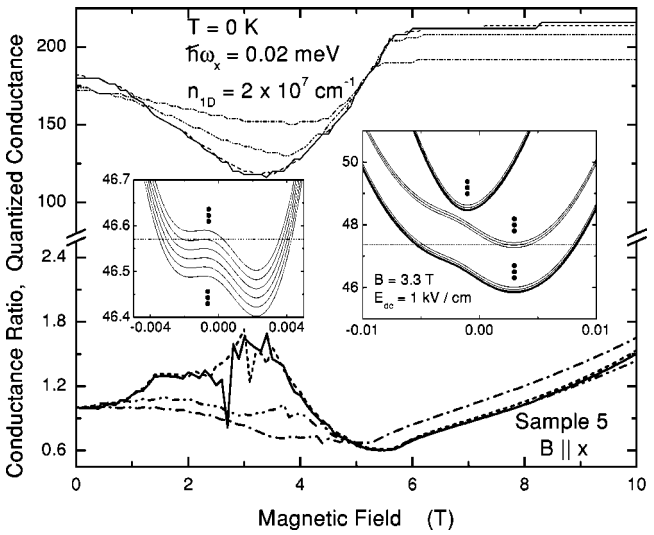

FIG. 8. $G_{yy}(B)/G_{yy}(0)$ (thick curves) and $\tilde{G}_{yy}(B)$ (thin curves) in unit of $2e^2/h$ for sample 5 with $n_{1D}=2\times10^7$ cm^{-1} at $T=0$ K as a function of B in the x direction. The sample is biased with a uniform dc field $E_{dc}=0$ (solid curves), 0.1 kV/cm (dashed curves), 0.5 kV/cm (dash-double dotted curves), and 1 kV/cm (dash-dotted curves). Here, $G_{yy}(0)=28.4e^2/h$ (thick solid curve), $27.7e^2/h$ (thick dashed curve), $26.4e^2/h$ (thick dash-double dotted curve), and $24.5e^2/h$ (thick dash-dotted curve) for $L_y=1$ μm.

electric fields $E_{dc}=0$ (solid curves), 0.1 kV/cm (dashed curves), 0.5 kV/cm (dash-double dotted curves), and 1 kV/cm (dash-dotted curves). A mismatch of about 1.3 meV is introduced between the wells by $E_{dc}=1$ kV/cm. The thick solid curve in Fig. 8 for $E_{dc}=0$ is the same as that in Fig. 5 and has a maximum at $B=3.3$ T. In this case, the structure is symmetric and a full symmetric hump is developed. This hump disappears as shown in the right inset at the same B when a severe energy mismatch is introduced through the bias $E_{dc}=1$ kV/cm, suppressing the conductance maximum as seen from the thick dash-dotted curve. The nearly flat quantized conductance for $E_{dc}=1$ kV/cm (thin dash-dotted curve) is the consequence of the absence of the full anticrossing gap where a sublevel can minimize its Fermi points from four to two, thereby minimizing the quantized conductance. This effect also suppresses the peak of $G_{yy}(B)/G_{yy}(0)$ due to the increased gap. In this case, only the lower branch is occupied at $B=0$, yielding the initial decrease of $G_{yy}(B)/G_{yy}(0)$ of the dash-dotted curve in Fig. 8, similarly to the behavior of the dashed curve in Fig. 7. At an intermediate field $E_{dc}=0.5$ kV/cm (thick dash-double dotted curve), the B dependence of the diffusive conductance is similar to the low-density (or strong-tunneling) case in Figs. 5–7. Note also that a small energy mismatch of 0.13 meV between the wells introduced by a small field $E_{dc}=0.1$ kV/cm (thick dashed curve) reduces the depth of the $E_{dc}=0$ dip of the diffusive conductance at 2.7 T and shifts it to 3.1 T. This is due to the fact that the flat $E_{dc}=0$ horizontal broad alignment of the energy-dispersion curves (shown in the inset of Fig. 5) which coincides with the Fermi level at $B=2.7$ T is somewhat tilted and less flat as shown in the left inset of Fig. 8 at $B=3.1$ T and occurs at a higher B in this case.

VII. CONCLUSIONS

We have investigated the quantized and diffusive magnetoquantum conductance for single and tunnel-coupled double wires which are wide ($\lesssim 1$ μm) in one perpendicular direction with densely populated sublevels and extremely confined in the other perpendicular (i.e., growth) direction. A general analytic solution to the Boltzmann equation was presented for multisublevel elastic scattering at low temperatures. The solution was employed to study interesting magnetic-field dependent behavior of the conductance such as the enhancement and the quantum oscillations of the conductance for various structures and field orientations. These phenomena originate from the following B-induced properties, namely, magnetic confinement, displacement of the initial- and final-state wave functions for scattering, variation of the Fermi velocities, mass enhancement, depopulation of the sublevels and the anticrossing (in double quantum wires). The magnetoconductance was found to be strikingly different in long diffusive (or rough, dirty) wires from the quantized conductance in short ballistic (or clean) wires. Numerical results obtained for the rectangular confinement potentials in the growth direction were satisfactorily interpreted in terms of the analytic solutions based on harmonic confinement potentials.

For a single quantum wire the magnetic field **B** was assumed to be either in the x or z direction. In either case, the quantized conductance is a monotonically decreasing function of B. When the magnetic field is in the x direction, perpendicular to both the growth direction and the wire, we found, for the interface-roughness scattering, that the diffusive conductance G increases as $\ln G \propto B^2$ at low B and as $\ln G \propto B$ at high B as shown in Fig. 2. However, the conductance is superimposed with rapid quantum oscillations shown in Fig. 3. The above low field behavior is due to the B-induced relative displacement in the z direction of the initial and final scattering states. On the other hand, the high-field conductance enhancement arises from the magnetic confinement of the initial and final wave functions away from the interfaces. The quantum oscillations in Fig. 3 are due to the channel-sublevel depopulation. In this case, the channel level separation $\hbar\omega_x$ is not affected by B. The depopulation is through the B-induced mass enhancement. Note that, by contrast, the quantized conductance decreases with B in this case. A very different behavior is obtained for the diffusive conductance when B is in the z direction as shown in Fig. 4. In this case, the conductance rises very rapidly at low B due to the relative displacement of the channel wave functions but the average conductance decreases at high B due to the shrinking orbit size.

For coupled double QW's, with B in the x direction, both the quantized and diffusive conductances show very different behavior from single QW's. The quantized conductance has a V-shaped B dependence, showing a minimum. The diffusive conductance shows very different B dependences, depending on whether both the upper and lower branches of the tunnel-split ground doublet are occupied (weak-tunneling, high-density limit) or only the lower branch is occupied (strong tunneling, low-density limit). In the former case, the

conductance rises with B, suddenly drops to a dip, rises again to a maximum, gradually decreases to a broad minimum and steadily rises in the high B limit as shown by the thick dashed and solid curves in Fig. 5 for symmetric double QW's. The high-B limit corresponds to the single QW limit where the electrons are localized in separate wells. The sudden drop of the conductance occurs when the Fermi level is coincident with one of the channel sublevels due to a flat bottom of the lower branch. The maximum of the diffusive conductance occurs due to the B-induced separation of the initial and final back-scattering states into the opposite wells when the chemical lies inside the gaps of the majority of the sublevels. The broad minimum arises from the large scattering rates associated with the large DOS at the lower gap edges of the last few channel sublevels which pass through the chemical potential. When only the lower branch is occupied at $B=0$, however, the diffusive conductance decreases initially with B as shown in Figs. 5 and 7. The behavior at higher B is the same as in the case where both branches are occupied at $B=0$. The conductance shows rugged features at low temperatures, reflecting the successive depopulation of the sublevels and is rounded at higher temperatures as shown in Fig. 6. The effect of the asymmetric wells was studied in Fig. 8 by applying a dc electric field. The asymmetry makes the quantized conductance minimum shallow. The diffusive conductance shows a similar behavior to the symmetric case where only the lower branch is occupied. This behavior of the diffusive conductance obtained for asymmetric wells as well as for the low-density or large-gap samples is consistent with that observed recently for long double quantum wires.[4] On the other hand, the V-shaped quantized conductance with a minimum as shown in Figs. 5–8 is similar to that observed[4,6] recently for short double quantum wires, suggesting that the transport may be ballistic for the samples. The B dependence of the diffusive conductance obtained for small $\hbar\omega_x$ is similar to that observed recently for *two-dimensional* double QW's except for the superimposed quantum oscillations and the dip.[8,10,18,19] The oscillations and the dip are the unique signatures of the discrete sublevels.

ACKNOWLEDGMENTS

The authors wish to thank J. S. Moon, J. A. Simmons, M. Blount, and J. L. Reno for numerous very helpful discussions on the subject. They are grateful to J. A. Simmons for a critical reading of the manuscript. Sandia is a multiprogram laboratory operated by Sandia Corporation, a Lockheed Martin Company, for the U.S. DOE under Contract No. DE-AC04-94AL85000.

[1] C. V. J. Beenaker and H. van Houton, in *Solid State Physics: Semiconductor Heterostructures and Nanostructures*, edited by H. Ehrenreich and D. Turnbull (Academic, New York, 1991), Vol. 44, and references therein.

[2] B. J. van Wees, L. P. Kouwenhoven, H. van Houten, C. W. J. Beenakker, J. E. Mooij, C. T. Foxon, and J. J. Harris, Phys. Rev. B **38**, 3625 (1988).

[3] D. A. Wharam, T. J. Thornton, R. Newbury, M. Pepper, H. Ahmed, J. E. F. Frost, D. G. Hasko, D. C. Peacock, D. A. Ritchie, and G. A. C. Jones, J. Phys. C **21**, L209 (1988).

[4] J. S. Moon, M. A. Blount, J. A. Simmons, J. R. Wendt, S. K. Lyo, and J. L. Reno, Phys. Rev. B **60**, 11 530 (1999).

[5] S. K. Lyo, Phys. Rev. B **60**, 7732 (1999).

[6] S. T. Stoddart, P. C. Main, M. J. Gompertz, A. Nogaret, L. Eaves, M. Henini, and S. P. Beaumont, Physica B **258**, 413 (1998).

[7] K. J. Thomas, J. T. Nicholls, M. Y. Simmons, W. R. Tribe, A. G. Davies, and M. Pepper, Physica B **59**, 12 252 (1999).

[8] J. A. Simmons, S. K. Lyo, N. E. Harff, and J. K. Klem, Phys. Rev. Lett. **73**, 2256 (1994).

[9] S. K. Lyo, Phys. Rev. B **50**, 4965 (1994).

[10] A. Kurobe, I. M. Castleton, E. H. Linfield, M. P. Grimshaw, K. M. Brown, D. A. Ritchie, M. Pepper, and G. A. C. Jones, Phys. Rev. B **50**, 4889 (1994).

[11] S. K. Lyo, J. Phys.: Condens. Matter **8**, L703 (1996).

[12] D. H. Huang and S. K. Lyo, J. Phys.: Condens. Matter **12**, 3383 (2000).

[13] S. V. Korepov and M. A. Liberman, Phys. Rev. B **60**, 13 770 (1999); Solid State Commun. **117**, 291 (2000), and references therein.

[14] J. M. Ziman, *Principles of the Theory of Solids*, 2nd ed. (Cambridge University Press, Cambridge, England, 1972), p. 215; W. Kohn and J. M. Luttinger, Phys. Rev. **108**, 590 (1957).

[15] H. Akera and T. Ando, Phys. Rev. B **43**, 11 676 (1991).

[16] S. K. Lyo, J. Phys.: Condens. Matter **13**, 1259 (2001).

[17] I. S. Gradshtyne and I. M. Ryzhik, *Table of Integrals, Series, and Products* (Academic Press, San Diego, 1980).

[18] M. A. Blount, J. A. Simmons, and S. K. Lyo, Phys. Rev. B **57**, 14 882 (1998).

[19] T. Jungwirth, T. S. Lay, L. Strčka, and M. Shayegan, Phys. Rev. B **56**, 1029 (1997).